The International Journal of Advanced Manufacturing Technology (2023) 129:5615–5624
https://doi.org/10.1007/s00170-023-12681-7

ORIGINAL ARTICLE

Mechanical and structural behavior of high-strength low-alloy steel pad welded by underwater wet welding conditions

Rassim Younes[1] · Jacek Tomków[2] · Abdelhak Idir[1] · Sarra Boudjit[1] · Mohand Amokrane Bradai[1]

Received: 12 June 2023 / Accepted: 13 November 2023 / Published online: 22 November 2023

Abstract

The aim of the paper was to determine the metallurgical and mechanical behaviors of a high-strength low-alloy (HSLA) steel pad-welded specimen used in the structures of industrial and naval parts. Then to predict the metallurgical consequences (nature of the phases present) and the mechanical properties (hardness and impact strength) of the pad-welded steel obtained by underwater wet welding with different heat input values. The XRD patterns clearly reveal a ferritic alpha steel S460N for both parameters. The ferritic quantification is above 70 wt% for low-alloy steel. The welded specimens are characterized by the presence of different phases. In a specimen performed with higher heat input, the complex oxide Mn_2TiO_4 was found to be around 7 wt%. Moreover, the solid solution formed with iron and manganese was observed. The hardness results obtained by indentation showed that the higher heat input resulted in higher hardness values (54 HRC) than for specimen performed with lower parameters (45 HRC). The impact test showed that the toughness of both pad-welded layers is greater than the toughness of the base material (40 kV for S2 and 34 kV for S1 about 27 kV for low-alloy steel). Moreover, it was observed that higher heat input results in increasing the impact strength of pad welds.

Keywords Underwater welding · High-strength low-alloy steel · X-ray diffraction · Hardness · Wet welding

1 Introduction

Welding processes generate thermal cycles that lead to phase transformations in the solid state in the heat affected zone (HAZ) and in the liquid state in the molten zone (MZ). These metallurgical changes depend on the local chemical composition of the base material and the welding conditions such as process parameters, welding environment, and cooling conditions [1–3]. Repair welding in the open air is a well-known process and often results in joints with good mechanical properties. However, it needs time and cost of transportation structures out of the water. A way to perform necessity repairs is wet welding directly under the water. Compared to other underwater welding methods such as dry welding [4] and local cavity welding [5], wet welding allows the process to be performed in the shortest time [6, 7]. However, direct contact with water generates some significant problems such as imperfections and the lower mechanical properties of underwater joints in comparison to joints made in the open air. The weldability of steel joints made in air conditions is often better than those made in the water [8–10]. However, there are some methods, which allow to improve the quality of underwater welded structures. A number of studies on changing the heat input values to improve the weldability have been reported [11–13]. Zhang et al. [14] compared the weld morphology and microstructure obtained from welding in water and in air. The results indicated that the real heat input during underwater welding was about 8% lower than in air. Because of the lower total heat input and higher cooling rate, the HAZ of underwater welds contained less pro-eutectoid ferrite (PF). Li et al. [15] determined that the width of the overheated zone in HAZ near the fusion line increased with the welding heat input in underwater wet welding of E40 steel using Ni based self-shielded flux-cored wires. Both the ultimate tensile strength and impact toughness increased through solid-solution hardening due to the dissolution of more alloying elements (e.g., Fe, Mn, and Cr).

✉ Jacek Tomków
jacek.tomkow@pg.edu.pl

[1] Laboratoire de Mécanique, Matériaux Et Énergétique (L2ME), Faculté de Technologie, Université de Bejaia, 6000 Bejaia, Algeria

[2] Faculty of Mechanical Engineering and Ship Technology, Gdańsk University of Technology, G. Narutowicza Street 11/12, 80-233 Gdańsk, Poland

Table 1 Chemical composition of S460N steel

Fe	C	Mn	Ni	S	P
Bal	0.16	1.51	0.05	0.0003	0.02

Gao et al. [16] noted that a low welding heat input generates better mechanical properties of the weld metal. However, it also increased the susceptibility to cold cracking in the HAZ. Hu et al. [17] welded duplex stainless steel with underwater local dry FCAW at different depths. The results showed that the austenite formation was reduced with increasing the water depth. It was connected with increasing heat dissipation at higher depth. Zhai et al. [18] reported that the amount of acicular ferrite (AF) transformed during various droplet transfer modes differed in underwater local cavity tungsten inert gas (TIG) welding using a flux-cored wire. The weld metal corresponding to the continuous liquid transfer mode with the lowest heat input contained more AF and less PF. Gao et al. [19] analyzed the influence of leading ultrasonic vibrations on the process forces in the friction stir welding with and without ultrasonic. It was found that the effect of ultrasonic vibrations on traverse force is more pronounced than that on the tool torque and axial force. The ultrasonic effect on welding forces is found to be governed by the travel speeds of both the tool and workpiece.

In this paper, the influence of the heat input values on the properties and chemical composition of underwater pad welds performed with covered electrodes was investigated. For studies, S460N high-strength low-alloy (HSLA) steel was selected. This material is characterized by high susceptibility to cold cracking in wet welding conditions, which was proved in previous investigations [20]. To the best of the author's knowledge, the influence of heat input on the pad weld properties and their chemical composition for HSLA steel in wet welded conditions with covered electrodes has not been investigated earlier.

2 Materials and experimental procedures

2.1 Materials used

Sheets of S460N HSLA steel of dimensions 150 mm × 100 mm × 12 mm were selected for research purposes. Steel's chemical composition and mechanical properties are presented in Tables 1 and 2. The chemical composition of the base material was analyzed by the spark emission spectrometry method with the usage of Metavision-1008i (Metal Power, India).

For the research, a special rutile electrode for underwater works (nearest equivalent E42 2 1 Ni RR 51) with a diameter of 4 mm was used. The chemical composition of filler material can be found in Table 3.

Table 2 Mechanical properties of the materials used following the manufacturer's data (certificate 3.1 in accordance to EN 10204)

Yield point, Re (MPa)	Tensile strength, Rm (MPa)	Elongation, A_{50} (%)
515	626	27.3

Table 3 Chemical composition of the weld deposit in Barracuda electrode in percent (%) following the manufacturer's data

Ti	C	Si	Mn	P	S
Bal	0.07	0.45	0.5	0.025	0.025

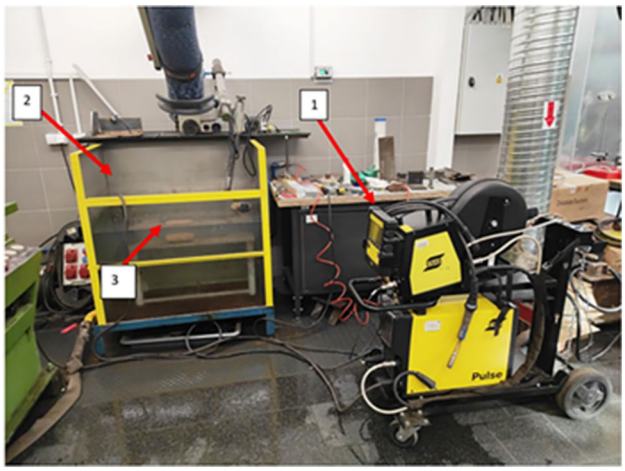

Fig. 1 The welding stand: 1—welding power source and wire feed unit, 2—tank, 3—welding table

2.2 Welding procedure

Welding was performed using the manual metal arc (MMA) method in a laboratory welding stand (Fig. 1).

According to the filler material manufacturer's recommendations, welding current with negative polarity (DC −) was used. The welding process was performed at the depth of about 150 mm in fresh water of temperature about 20 °C. Welding parameters were selected following manufacturer data and preliminary investigations. They allow the creation of a stable welding arc during the process. Samples were welded with different heat input values to compare the influence of this parameter on the quality of wet-welded layers. The heat input values were calculated following Eq. 1. The coefficient "k" equal to 1 was used, which is commonly used

Table 4 Parameters used to weld samples

Code	S1	S2
I (A)	195	272
U (V)	26	25.75
Vsp (mm/s)	8.2	7.1
ql (kJ/mm)	0.62	0.99

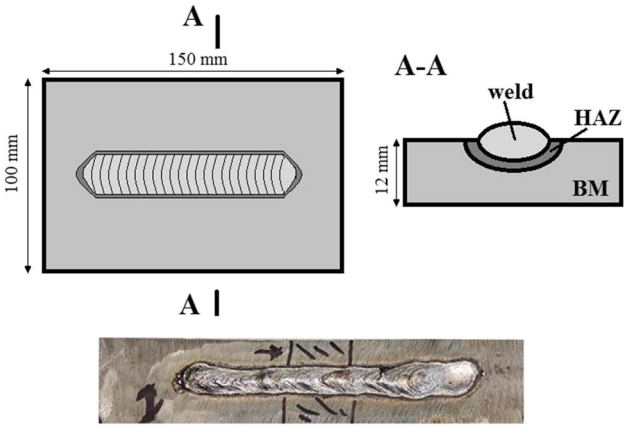

Fig. 2 Scheme of specimens and real view of sample after welding and initial cutting for metallographic tests

for underwater welding, because its value is unknown in the water environment [12, 20].

$$ql = k \times (U \times I)/Vsp \quad (1)$$

in which: ql—heat input (kJ/mm), U—voltage (V), I—welding current (A), Vsp—welding speed (mm/s).

The welding speed was calculated using the following procedure (Eq. 2) and presented in Table 4. Firstly, the length of pad weld, and the welding time were measured.

$$Vsp = l/t \quad (2)$$

in which: Vsp— welding speed (mm/s), l—weld length (millimeter), t—welding time (seconds).

Welding parameters are presented in Table 4.

Testing welds were laid following the scheme presented in Fig. 2.

2.3 Microstructural and structural characterization

The microstructural analysis and identification of the phases was obtained by using the scanning electron microscopy (SEM) and XRD diffraction. The surface of samples was ground using SiC paper with different gradation and finally polished. Microstructures were observed on specimen surfaces and in cross sections using a scanning electron microscope (SEM, JEOL brand type JSM6360LV, Japan). The X-ray diffraction patterns were recorded using diffractometer X'PERT PRO MRD (MALVERN PANalytical, UK), equipped with a copper anode X-ray tube and a curved graphite monochromator in the diffracted beam set of Cu K radiation, which includes the Kα1 and Kα2 α wavelengths. The strong presence of defects in these materials creates a significant background noise; to improve counting statistics and increase the peak/background ratio, an acquisition time of 40 s per angular step of 0.04° and a count time of 5 s per step has been used in the interval ranging between 10 and 110° (2θ). The identification of the crystal phases was performed by comparison of the observed lines with those appropriate phases contained in the database ICDD-PDF2.

2.4 Mechanical characterization

2.4.1 Hardness test

The Rockwell hardness measurements were performed on the polished surface of pad welds using hardness tester ZHV10 type (Zwick, Germany) under a load of 293 Kgf and a dwell time of 15 s. The loading and unloading speeds were 0.5 mm/min and 0.1 mm/min, respectively. For each indentation test, the computer-controlled device provides, according to the Test Xpert software. An average hardness was calculated from 5 measurements per specimen.

2.4.2 Charpy test

The Charpy test was performed in accordance with EN 10045 standard at impact velocity 5.52 m/s [21] (Charpy test Metrotec brand type PIT-25, UK). The test method involves impacting a standard test piece with a falling mass, which is free to rebound after impact. In this method, a pendulum impact is provided at its end with a knife, it develops a given energy at the impact. The equipment used in a pendulum machine is equipped with a clamping device, a centering reference of test specimens, and a meter on which you can read the energy in joules after the rupture of the specimen. The samples of high-alloy chromium-cast iron balls have a dimension of $10 \times 10 \times 55$ mm^3, the angle through which the samples move before impact is set to V-notch 45°. The energy absorbed by the specimen is calculated by the following equation, Eq. 3:

$$W = P(h0 - h1) \quad (3)$$

The impact resistance K_{cv} is equal to W/S [J/cm^2].

P load (N),

h height (meters),

Kcv impact resistance (J/cm^2)

2.4.3 Waviness profile determination

To test the waviness profile, the sample was clean and secured onto a stable surface using clamps. Th111e roughness characteristics of all test specimens were measured by using high-sensibility contact by equipment Veeco dektak 150 stylus profiler. The profilometer was calibrated according to these parameters: L cutoff: 0.25 mm, speed: 0.5 mm/s, N. cutoff: 5, Filter: Gaussian. Then an appropriate stylus was mounted, considering the characteristics of the surface being tested (e.g., surface finish and material hardness). Accordingly, the roughness information was taken from an area of 130 mm to 42 mm. Results of the two measurements for each roughness profile were initially averaged by the device's software and recorded for the subsequent analysis. The extracted waviness profile was used to assess the surface's characteristics. This may involve quantifying parameters such as waviness amplitude, wavelength, and form.

3 Results and discussion

3.1 SEM images

Figure 3 shows the cross sectional optical macroscope images of the welded joint obtained in the water environment.

In the visual testing, no surface imperfections were observed in the middle areas of both specimens. However, partial start and finish defects were observed in the joints on the last pass, especially in specimen S2 welded with higher heat input values. Some typical [6, 19] underwater welding imperfections (wrong geometry) were found in specimen S1 (Fig. 4). Moreover, the width of the weld bead of the joint obtained under higher heat input values (S2) was larger than that of the specimen S1. It resulted from limited visibility in the water environment. Figure 4 presents SEM pictures of the specimens. As seen in Fig. 4, there were a number of burn-through defects on the side of the weld bead of both specimens. However, less macro- and microcracks were observed in specimen S1, which was expected following previous investigations of S460N steel [6]. Ultrasonic tests showed lack of penetration in some areas of sample S1, but compared to the sample S2, the S1 is characterized by higher quality. In recent research, the impact of various process parameters on the microstructure in arc welding for mild steel was examined. According to Jin-Hyeong Park et al. [22], process parameters, which encompassed factors such as root gap distance, travel speed, and weaving, emerged as the primary influencers affecting both back-bead formation and microstructural characteristics. The accumulation of the molten pool was found to play a significant role in creating a cushioning effect at the center of the arc. Regarding the microstructures found in the weld metal, they predominantly consisted of acicular ferrite, along with some presence of grain boundary ferrite. However, when weaving was incorporated, it was observed that the microstructure within the HAZ primarily encouraged the formation of ferrite and pearlite. In contrast, in instances where weaving was not employed, the microstructure within the HAZ tended to promote the development of coarse bainite, accompanied by a certain amount of ferrite and martensite.

The significant difference in the components of the microstructure of the cross-section of the same welded joint of S1 or S2 can be explained through various factors that influence the welding process and subsequent microstructure formation. The most fundamental reason for the difference in microstructure components resulted from the composition of the materials being welded. S1 and S2 likely have the same chemical compositions but different in ratio; this difference of ratio is due to welding involving applying heat to melt and fuse the base materials. The specific welding process parameters and heat input differences between specimens resulted in different conditions of the materials melting, solidifying, and cooling, ultimately affecting microstructure formation. The diffusion of atoms within the material is a critical process during cooling and solidification. Higher heat input

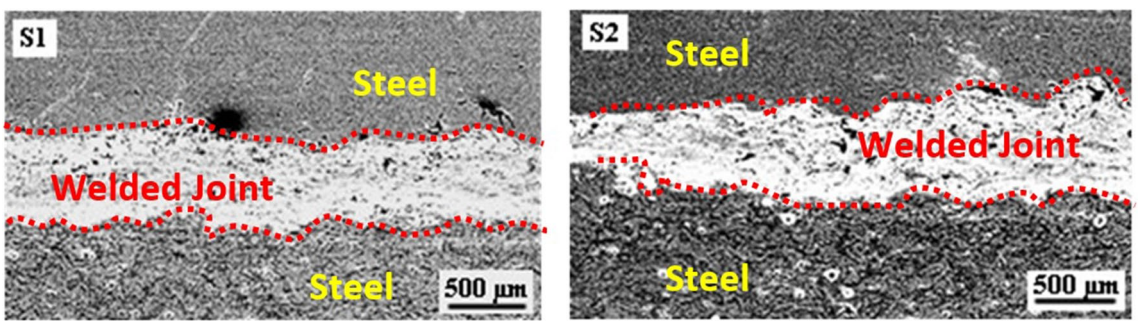

Fig. 3 Optical macroscope images of the transverse cross-section of a welded joint; S1—specimen S1, S2—specimen S2

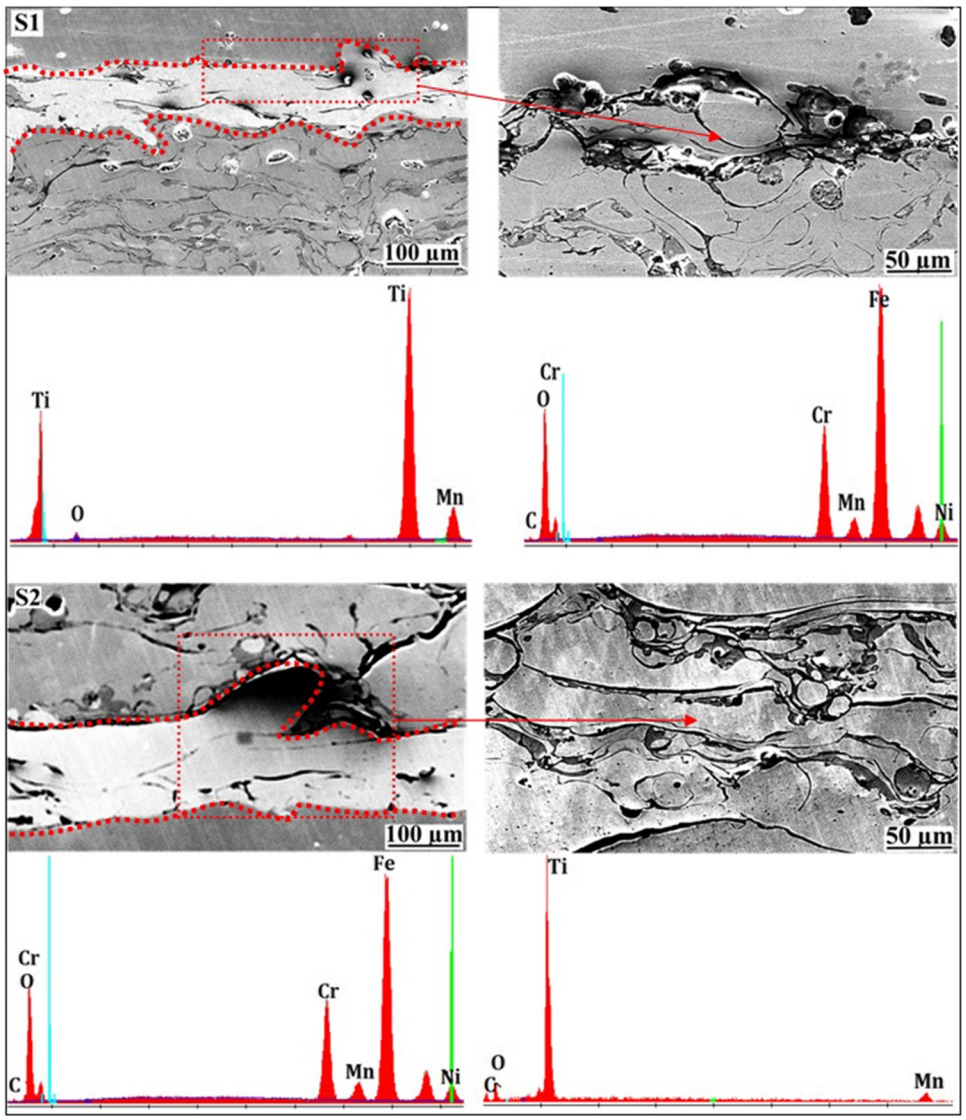

Fig. 4 SEM details showing the microstructure of the transverse cross-section of a welded joint

resulted in higher diffusion in the welding joint for specimen S2 (Sect. 3.2). Differences in diffusion rate can impact the distribution of alloying elements within the microstructure. Moreover, the HAZ received more energy (by higher heat input) in S2 which affects greater movement of elements like Mn on gradients microstructure of HAZ.

3.2 X-ray diffraction test

The XRD pattern pictures of the performed specimens are presented in Fig. 5.

The observed identification of the S460N steel revealed the presence of two phases: a majority phase of ferrit-α cubic centered structure (JCPDS n° 00–001-1262) with lattice parameter (a = b = c = 2.8608, all angles = 90°). The secondary identified phase is solid solution constituted mainly with iron and small amount of manganese characterized by cubic structure (JCPDS n° 03–065-7528) the lattice parameter of these crystallite is (a = b = c = 2.8607, angles = 90°), and their chemical formula is $Fe_{19}Mn$. Moreover, the spectrum presents a small amount of iron carbides, which is comprehensive with the steelmaking process (iron and carbides).

The XRD test also showed the presence of the same matrix in both specimens, due to diffusion and the thinness of welding given a cloudy recording element. However, the appearances of two small picks on 47.6 and 56.612° in the S1 sample were found. The first one was identified as a solid solution formed from diffusion between (Ti, Fe, and Mn) phases. It is characterized by the presence of cubic structure (JCPDS n° 01–082-1298). The second phase is a monoclinic crystal system with space group C2/m (JCPDS n° 00–046-1237).

On the other hand, the matrix of metallic substrate of underwater welding in specimen S2 was the same. The first majority phase is a ferrite-α cubic centered structure (JCPDS n° 00–001-1262) with lattice parameters (a = b = c = 2.8608,

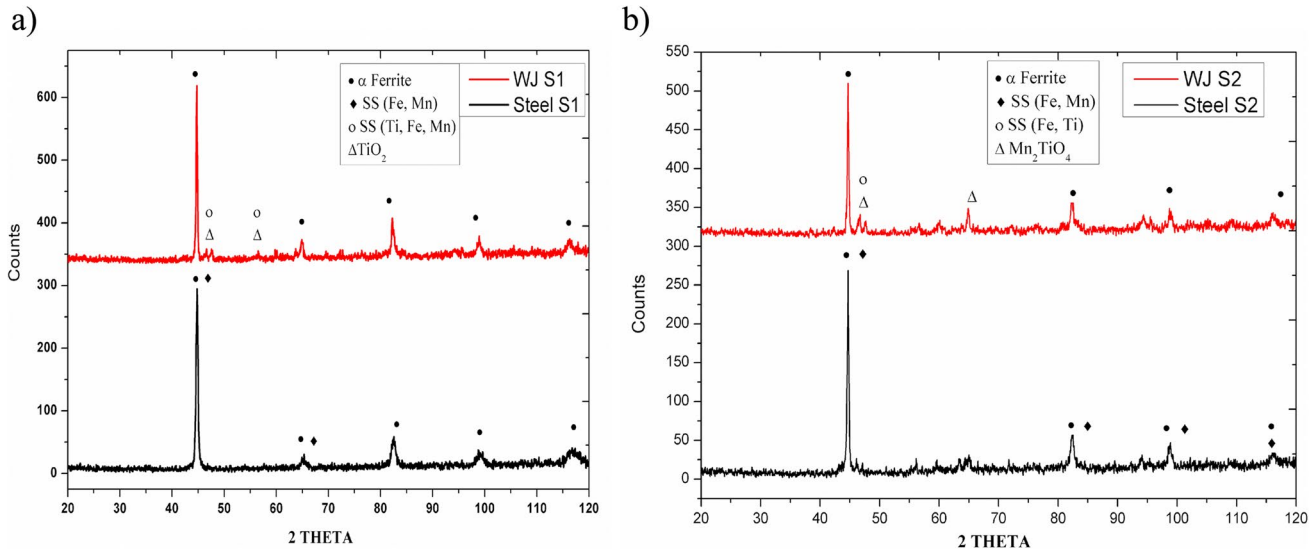

Fig. 5 X-ray diffraction spectrum of the **a** sample S1 and **b** sample S2

all angles = 90°). The secondary phase is a solid solution consisting mainly with iron and small amounts of manganese. It is characterized by a cubic structure (JCPDS n° 03–065-7528); the lattice parameter of these crystallites is (a = b = c = 2.8607, all angles = 90°). However, in the spectrum of specimen S2, characterized with the same shape, the two picks (47.6 and 56.612°) with greater intensity and higher crystallization than a pick of specimen S1, were observed. Tested weld metal of S2 also includes a complex oxide Mn_2TiO_4 (JCPDS n° 00–019-0795) and the other phases of solid solution formed just with iron and manganese. This may be caused by the influence of higher heat input during performing sample S2. Higher energy provides the formation of the oxide between Ti and Mn simultaneously with the disappearance of rutile phase. The Ti atoms are dissolved in other phases.

The structural quantification of phases of both samples is plotted in Fig. 6. The X-ray diffraction spectra of the low-alloy steel is revealed in Sect. 3.2. The presence of a main phase is identified with a major amount neatly 70% content for the two parameter welding. The quantification of phases of welding showed some diffusion on atoms for sample S1 and S2 zones. We note clearly the changes occur for the ferrite phase, which is a minor amount of 40% for sample S1 and 30% for sample S2. The most phases present in the welding zone is FeTiMn for S1 (content 54%) and FeTi (content 63%) for S2 becomes very dominant. It was noticed from the identification phases that there was a lack of Mn atoms in the solid solution in sample S2. The treatments carried out different heat input values to favor a diffusion; one also notes the presence of the form of an complex carbide Mn_2TiO_4 under parameter S2 about 7% was also observed. In the case of S1, the feedstock rutile appeared with a low composition. From quantification of phases, it clearly appeared the effect of parameter in diffusion of atoms of manganese, it allows to form small amount of complex carbides, and enhance the mechanical properties; in contrast, we found in parameter S1 the atoms of manganese is hold in solid solution and could not bilk the welding zone.

3.3 Mechanical characterization

3.3.1 Rockwell hardness measurements

The hardness of the various zones of both specimens was measured by Rockwell indentation with a load of 391 Kgf during 30 s. For each processing, the calculated average standard deviation is based on the average of 6 measurements. The results of hardness measurements following the distance from the top of layers are illustrated by the histogram in Fig. 7.

From the top of both samples to 3 mm depth, the hardness is similar with an average of 57 for specimen S2 and 54 for S1. Between 4 and 7 mm depth, the hardness decreases. However, the differences were observed with an average 45 HRC in specimen S1 and 52 HRC in specimen S2, which confirmed differences in microstructures observed in previous tests. From 8 mm depth, measurements were taken in the substrate, and the hardness of both specimens is similar, equal to the hardness of S460N steel. The sample S2 performed with higher values of heat input is characterized by higher hardness, which resulted from the segregation of elements that form phases that harden or soften the material. The hardening mechanisms in crystalline materials are varied and therefore result from a decrease in the mobility of dislocations. Hardening a metal therefore makes it

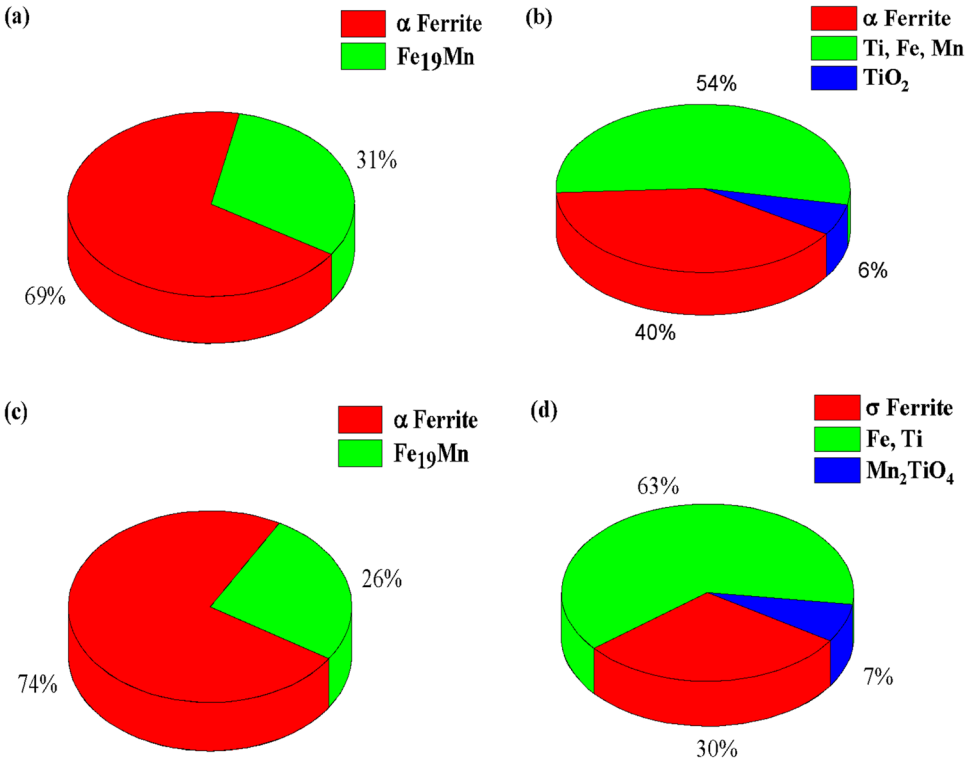

Fig.6 Quantification phases of samples: **a** low-alloy steel S1, **b** welding zone S1, **c** low-alloy steel S2, and **d** welding zone S2

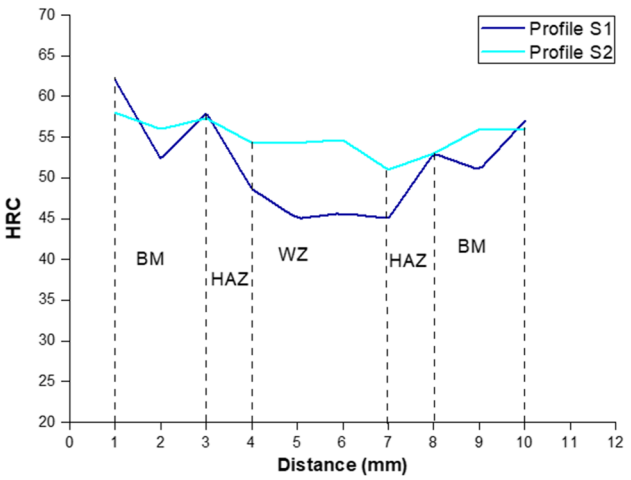

Fig. 7 Profile of hardness HRC of samples welded with parameters S1 and S2

potentially more brittle. One of the causes of hardening can be attributed to interactions between dislocations. Indeed, when deformation starts, the numerous dislocations created will interact to form an entanglement. The dislocations eventually become immobilized and the movement of new dislocations is considerably hindered as they pass through this "forest" of immobile dislocations [23, 24].

From X-ray diffraction, Sect. 3.1, it clearly shows the diffusion of element magnesium from matrix formed by steel to the welding joint did not allow enough energy to move in specimen S1. Moreover, this sample has more ability to form combined oxide with rutile than in specimen S2, where the amount of energy provides a deep modification on the inner structure of the welded layer, which formed harder phase Mn_2TiO_4.

3.3.2 Charpy test

Impact tests are performed on both samples S1 and S2. The results of Charpy impact tests are presented in Fig. 8. It was found that specimen S2 is characterized by higher toughness than specimen S1. This is due to the formation of complex fine carbide Mn_2TiO_4 type in S2, which therefore promotes the impact resistance. Ni et al. [25] investigated the effects of welding parameters on residual stresses. It was stated that longitudinal tensile residual stresses and transverse compressive residual stresses were observed in the vicinity of the weld zone joints. Moreover, it was found that in joints produced with a higher welding speed (lower heat input), both the longitudinal and transverse residual stresses were slightly higher compared to joints welded using lower welding speed values. These findings may be one potential reason why specimen S2 is characterized by higher K_V about 40 (J/Cm^3) compared to S1 (35 J/cm^3).

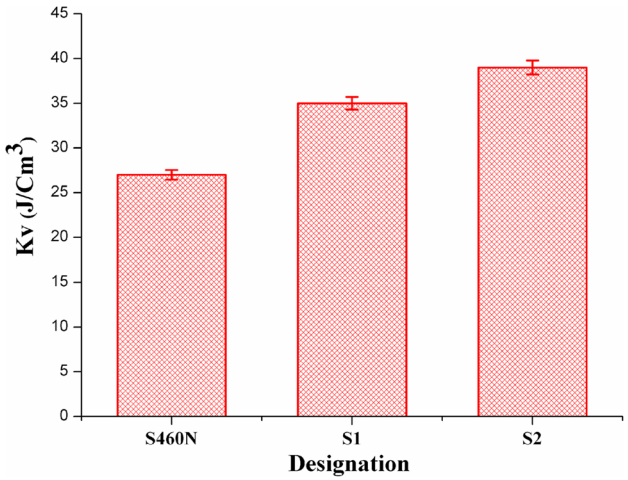

Fig. 8 Impact test of samples welded with parameters S1 and S2

3.3.3 Waviness analysis

The waviness profiles were depicted in Fig. 9 of the two samples welded with different tension parameters. Based on the provided surface roughness parameters, Ra (average roughness), Rq (root mean square roughness), Rt (maximum peak-to-valley height), and Rmax (maximum peak height) are mentioned in Table 5. Data was analyzed with an in-house code.

Although the evaluation length used in the calculations was equal to the traverse length. The selection of the sampling length, which is defined as the distance over which the surface parameters are assessed, is of critical importance since this length should include enough surface data within it to ensure a reliable statistical calculation and enable the removal of the waviness [18]. Three different sampling lengths of 5 mm, 30 mm, and 50 mm were considered in this study among them. This is due to the fact that a practical solution to ship hull roughness measurement works based on a height parameter accepted as ISO standards [26].

The first sample (S1) has an average deviation of the surface from the mean line roughness (Ra) of 0.302 µm. The root mean square roughness (Rq) is slightly higher at 0.394 µm, suggesting a higher variation in the surface roughness across the measured area. But the maximum vertical distance between the highest peak and the lowest valley in

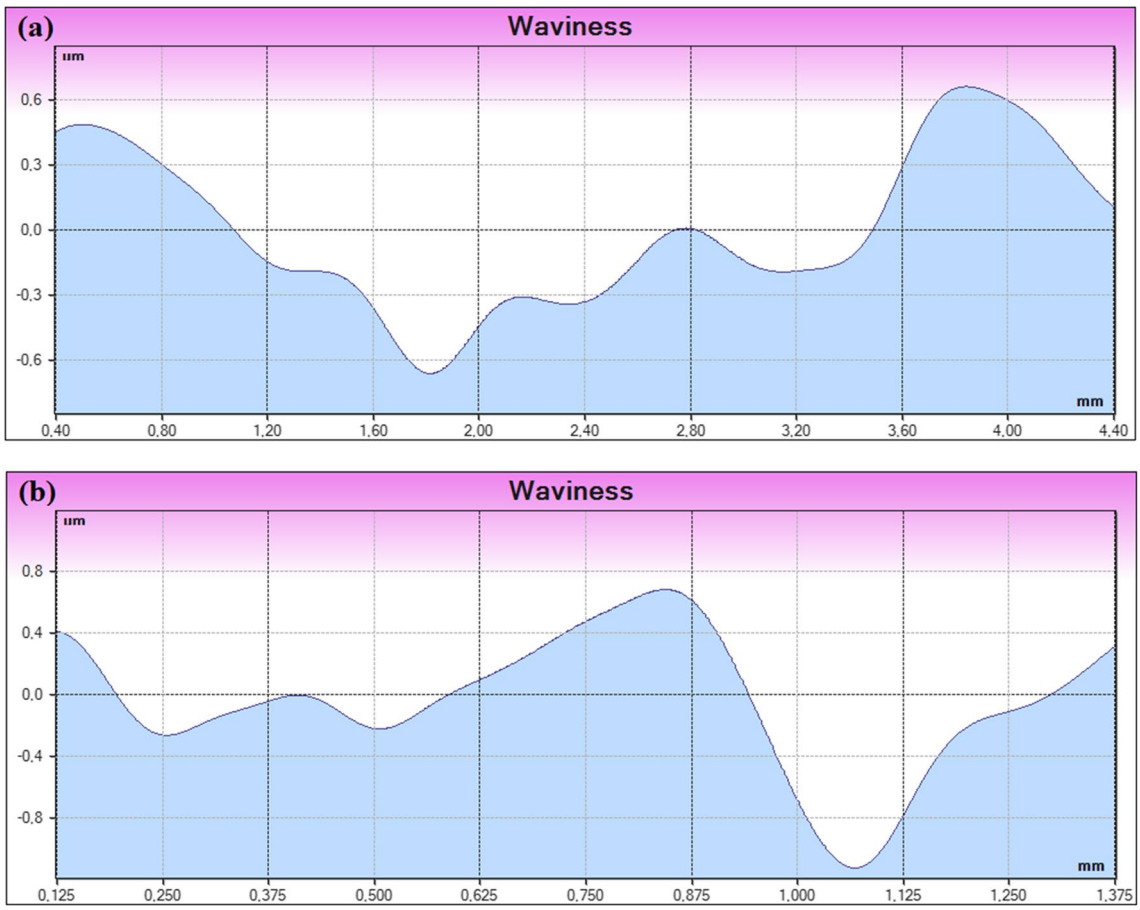

Fig. 9 Waviness test profile **a** S1 and **b** S2

Table 5 Roughness recorded of samples S1 and S2

Parameter	S1	S2
R_a (µm)	0.302	0.261
R_q (µm)	0.394	0.330
R_t (µm)	3.833	2.310
R_z (µm)	2.461	1.683
R_c (µm)	1.076	0.921
R max (µm)	3.727	2.769
RS_m (µm)	44.9	32.1
RP_c (/cm)	310	448

the surface profile (Rt) is 3.833 µm; this indicates significant height variations on the surface of the first sample. Whereas, the second sample (S2) has a lower average roughness (Ra) of 0.261 µm compared to the first sample, indicating a relatively smoother surface. The root mean square roughness (Rq) is also lower at 0.330 µm, suggesting less variation in roughness across the measured area. We note Rt is the lowest valley compared to the first sample, the maximum peak-to-valley height is 2.310 µm. This suggests a more consistent surface profile with fewer extreme height variations.

4 Conclusions

Performed investigations focused on the underwater pad welding process, which was carried out with direct contact with the water by wet welding method. The results of the investigations showed a significant effect of the welding parameters on the structural and hardness resistance of the produced layers, which has not been so deeply investigated yet. The effect was observed for both specimens S1 and S2, which were welded in the water with different values of heat input. The performed examinations allow us to draw the main conclusions:

1. The observed identification of the steel S460N revealed the presence of two phases: a majority phase of ferrite-α cubic centered structure (near 70 wt% for S1 and S2), the secondary phase is solid solution constituted mainly with iron and a small amount of manganese having cubic structure (less than 30 wt%).
2. The X-ray diffraction shows clearly the difference of oxides formed in wet-welded specimens. They present the same shape; however, the remark was the two picks (47.6 and 56.612°) which had more intensity and more crystallization than a pick obtained under welding specimen S1 made by lower heat input value. The phase formed in specimen S2 is a complex oxide Mn_2TiO_4. For S2, it was not observed in specimens welded with lower heat input.
3. The hardness in the water environment depends on the heat input (54 HRC for S2 rather than 45 HRC S1).

   The complex oxides appear on X-ray diffractograms, resulting from greater energy transferred to the specimen S2 (40 kV for S2 and 34 kV for S1).
4. It was confirmed that the toughness of underwater welded structures is strongly connected with welding parameters. The sample carried out with S1 has a roughness of 0.302 µm whereas the second sample (S2) has a lower roughness (Ra) of 0.261 µm.
5. To achieve a wider knowledge about properties of underwater welded structures, the next investigations should focus on fatigue life and hydrogen embrittlement. Moreover, the novel investigations of the tribological and electrochemical behaviors of low-alloy steel pad wet-welded layers will be carried out.

Acknowledgements The work described in the present paper has been developed within the project between our two laboratories. We would like to thank both institutions for collaboration.

Author contribution All authors contributed to the study conception and design. Material preparation, data collection, and analysis were performed by all authors, the same as the first draft of the manuscript was written. All authors commented on previous versions of the manuscript. All authors read and approved the final manuscript.

Declarations

Competing interests The authors declare no competing interests.

References

1. Wang F, Yang X, Cui L, Yin Y (2016) Fabricating defect-free API X65 steel welds under underwater wet conditions using friction taper plug welding. Mater Manuf Process 31:2123–2129. https://doi.org/10.1080/10426914.2016.1176194
2. Ratnayake RC, Brevik VA (2014) Experimental investigation of underwater stud friction stir welding parameters. Mater Manuf Process 29:1219–1225. https://doi.org/10.1080/10426914.2014.930891
3. Yang CW, Jiang SJ (2019) Weibull statistical analysis of strength fluctuation for failure prediction and structural durability of friction stir welded Al–Cu dissimilar joints correlated to metallurgical

bonded characteristics. Mater 12:205. https://doi.org/10.3390/ma12020205
4. Chen M, Yang K, Wang Z, Wang S, Wu E, Ni Z, Lu J, Sun G (2023) Underwater laser directed energy deposition of NV690 steel. Adv Pow Mater 2:100095. https://doi.org/10.1016/j.apmate.2022.100095
5. Hu Y, Shi Y, Wang K, Huang J (2023) Effect of heat input on microstructure and mechanical properties of local dry underwater welded duplex stainless steel. Mater 16:2289. https://doi.org/10.3390/ma16062289
6. Fydrych D, Raczko P, Świerczyńska A, Landowski M, Wolski A, Rogalski G (2023) Effect of arc strikes on high strength low alloy steels welded by SMAW. Adv Sci a Technol Research J 17:160–169. https://doi.org/10.12913/22998624/166061
7. Klett J, Hassel T (2020) Influence of stick electrode coating's moisture content on the diffusible hydrogen in underwater wet shielded metal arc welding. Adv Mater Sci 20:27–37. https://doi.org/10.2478/adms-2020-0020
8. Brätz O, Klett J, Wolf T, Henkel K-M, Maier HJ, Hassel T (2022) Induction heating in underwater wet welding—thermal input, microstructure and diffusible hydrogen content. Mater 15:1417. https://doi.org/10.3390/ma15041417
9. Shi Y, Hu Y, Yi Y, Lin S, Li Z (2017) Porosity and microstructure of underwater wet FCAW of duplex stainless steel. Metal Micro Analys 6:383–389. https://doi.org/10.1007/s13632-017-0376-3
10. Wang J, Sun Q, Pan Z, Yang J, Feng J (2019) Effects of welding speed on bubble dynamics and process stability in mechanical constraint-assisted underwater wet welding of steel sheets. J Mater Process Technol 264:389–401. https://doi.org/10.1016/j.jmatprotec.2018.09.022
11. Tomków J, Landowski M, Fydrych D, Rogalski G (2022) Underwater wet welding od S1300 ultra-high strength steel. Mar Stru 81:103120. https://doi.org/10.1016/j.marstruc.2021.103120
12. Tomków J, Landowski M, Rogalski G (2022) Application possibilities of the S960 steel in underwater welded structures. Facta Universitatis Series: Mech Eng 20:199–209. https://doi.org/10.22190/FUME210722066T
13. Tomków J, Świerczyńska A, Landowski M, Wolski A, Rogalski G (2021) Bead-on-plate underwater wet welding on S700MC steel. Adv in Sci and Technol Research J 15:288–296. https://doi.org/10.12913/22998624/140223
14. Zhang Y, Jia C, Zhao B, Hu J, Wu C (2016) Heat input and metal transfer influences on the weld geometry and microstructure during underwater wet FCAW. J of Mater Process Technol 238:373–382. https://doi.org/10.1016/j.jmatprotec.2016.07.024
15. Li H, Liu D, Yan Y, Guo N, Liu Y, Feng J (2018) Effects of heat input on arc stability and weld quality in underwater wet flux-cored arc welding of E40 steel. J of Manuf Process 31:833–843. https://doi.org/10.1016/j.jmapro.2018.01.013
16. Gao W, Wang D, Cheng F, Di X, Deng C, Xu W (2016) Microstructural and mechanical performance of underwater wet welded S355 steel. J Mater Process Technol 238:333–340. https://doi.org/10.1016/j.jmatprotec.2016.07.039
17. Hu Y, Shi Y, Sun K, Shen X (2019) Microstructure evolution and mechanical performance of underwater local dry welded DSS metals at various simulated water depths. J Mater Process Technol 264:366–376. https://doi.org/10.1016/j.jmatprotec.2018.09.023
18. Zhai Y, Yang L, He T, Liu Y (2017) Weld morphology and microstructure during simulated local dry underwater FCTIG. J Mater Process Technol 250:73–80. https://doi.org/10.1016/j.jmatprotec.2017.07.010
19. Gao S, Wu CS, Padhy GK (2019) Effect of leading ultrasonic vibrations on the welding forces of friction stir lap welding. Int J Adv Manuf Technol 104:3181–3189. https://doi.org/10.1007/s00170-019-04264-2
20. Tomków J, Janeczek A, Rogalski G, Wolski A (2020) Underwater local cavity welding of S460N steel. Mater 13:5535. https://doi.org/10.3390/ma13235535
21. Rogalski G, Łabanowski J, Fydrych D, Tomków J (2014) Bead-on-plate welding on S235JR steel by underwater local dry chamber process. Polish Maritime Res 21:58–64. https://doi.org/10.2478/pomr-2014-0020
22. Park JH, Kim SH, Moon HS et al (2020) Effect of process parameters on root pass welding and analysis of microstructure in V-groove pulsed gas metal arc welding for mild steel. Int J Adv Manuf Technol 109:1969–1985. https://doi.org/10.1007/s00170-020-05736-6
23. Riyanta B, Wardana ING, Irawan YS, Agus Choiron M (2017) AISI 304 welding fracture resistance by a Charpy impact test with a high speed sampling rate. Met 7:543. https://doi.org/10.3390/met7120543
24. Kapp JA, Underwood JH (1992) Correlation between fracture toughness, Charpy V-notch impact energy, and yield strength for ASTM A723 steel. Me-Morandum Report ARCCB-MR 92008. Wateviled, New York
25. Ni Y, Qin DQ, Mao Y et al (2020) Influences of welding parameters on axial force and deformations of micro pinless friction stir welding. Int J Adv Manuf Technol 106:3273–3283. https://doi.org/10.1007/s00170-019-04739-2
26. Terán G, Capula-Colindres S, Angeles-Herrera D, Velázquez JC, Fernández-Cueto MJ (2016) Estimation of fracture toughness KIC from Charpy impact test data in T-welded connections repaired by grinding and wet welding. Eng Fract Mecha 153:351–359. https://doi.org/10.1016/j.engfracmech.2015.12.010